Optical Materials 112 (2021) 110780

Contents lists available at ScienceDirect

Optical Materials

journal homepage: http://www.elsevier.com/locate/optmat

Research Article

The Correlation between Structural and Optical Properties of Zinc Hydroxide Nanoparticle in Supports Photocatalytic Performance

Nurlaela Rauf [a], Sultan Ilyas [a], Heryanto Heryanto [a], Roni Rahmat [a], Ahmad Nurul Fahri [a], Mufti Hatur Rahmi [b], Dahlang Tahir [a,*]

[a] Department of Physics, Hasanuddin University, Makassar, 90245, Indonesia
[b] Department of Fisheries, Hasanuddin University, Makassar, 90245, Indonesia

ARTICLE INFO

Keywords:
FTIR
Optical properties
UV-VIS
Structural properties
Photo-catalytic
Zn(OH)2

ABSTRACT

- Green synthesized Zn(OH)2 mediated by Coleus blumei Benth leaf for pH: 4, 7, 10 and for calcination temperature: 400 °C, 450 °C, 500 °C, 550 °C, and 600 °C have been characterized by using Fourier transform infrared (FTIR), ultraviolet–visible (Uv–Vis), and X-ray diffraction (XRD). The bonding formation present Zn–*O*–H, H–*O*–H, *O*–H, and Zn–O indicated Zn(OH)2 nanocrystal successfully synthesized. The optical, dielectric properties, and energy loss function were quantitatively determined from the FTIR spectra by using Kramers-Kronig (KK) dispersion relation. The distance between longitudinal (LO) and transverse (TO) optical phonon vibration mode Δ (LO-TO) and the bandgap increases with increasing the calcination temperature for all pH due to the amount of covalent bond is increase. The best calcination temperature is 600 °C and pH 7 indicated by the rate of the degradation performance is faster than the other temperature and pH. In this study shows FTIR spectra effective ways for determining the optical and dielectric properties, optical phonon vibration mode, and energy loss function of Zn(OH)2 material.

1. Introduction

The nanoparticle is an important area of research due to the application in all fields of human life: medical, pharmacy, engineering, and material sciences. Methods of synthesized nanoparticle were various from the high technology: molecular beam epitaxial [1], atomic layer deposition [2], lithography [3], laser ablation [4], photonics [5], chemical reaction [6], sputtering [7], and also simple technology by green approach [8]. All of these synthesized methods are expensive and hazardous to the environment except for the green approach [8–10]. The green approach or biological methods for synthesis nanoparticle have been reported by many researchers [8–12] due to the low cost and environmentally friendly [10–12]. Green synthesized usually used leaves of the plant, vegetables, microbes, and gum which were abundant in nature [10–15]. Nanoparticle for photo-catalyst application was reported for removal waste industries; methyl orange [16], methyl blue [17], tetracycline [18], pesticide [19], Indigo Carmine [20], and *p*-Nitrophenol [21,22]. The waste from the textile industries in the form of phenol is easily flow in the water and absorbing in the soil which indirectly can damage the surface water, groundwater, soil, and vegetation.

There are many researchers also reported that, the materials that can be used for removing the harmful chemical from the liquid such as; Bi12TiO20 [16], Titanate Nanotube (TNT) [17], ZrO2 [20], CdTe/TiO2 [21], Mg/ZnO [22], Ag2SO4/ZnO [23], MoS2 [24], Ga/ZnO [25], and ZnO [26]. Recently, reported in Refs. [27–31] shows that the zinc hydroxide (Zn (OH)2) has been widely used for catalytic and optical devices applications due to the high similarity properties with ZnO such as high electron mobility, high intrinsic impurities, and present several types of defect, including oxygen and hydrogen vacancy, zinc interstitial, and oxygen interstitials [28]. However, the optical properties, dielectric properties, energy loss function, and structural properties are the most essential knowledge to understand the best characteristics of Zn(OH)2 nanoparticle for various applications that have not been experimentally investigated adequately.

In this study, we applied biological methods by using aqueous extract of Coleus blumei Benth leaf as a biological reagent for the synthesis of Zn (OH)2 nanocrystal by varying the calcination temperature (400 °C, 450 °C, 500 °C, 550 °C, and 600 °C) and the pH (4, 7, 1st 10). The Kramers-Kronig (KK) dispersion relation was used for determining the

* Corresponding author.
E-mail address: dtahir@fmipa.unhas.ac.id (D. Tahir).

https://doi.org/10.1016/j.optmat.2020.110780
Received 5 December 2020; Accepted 22 December 2020
Available online 7 January 2021

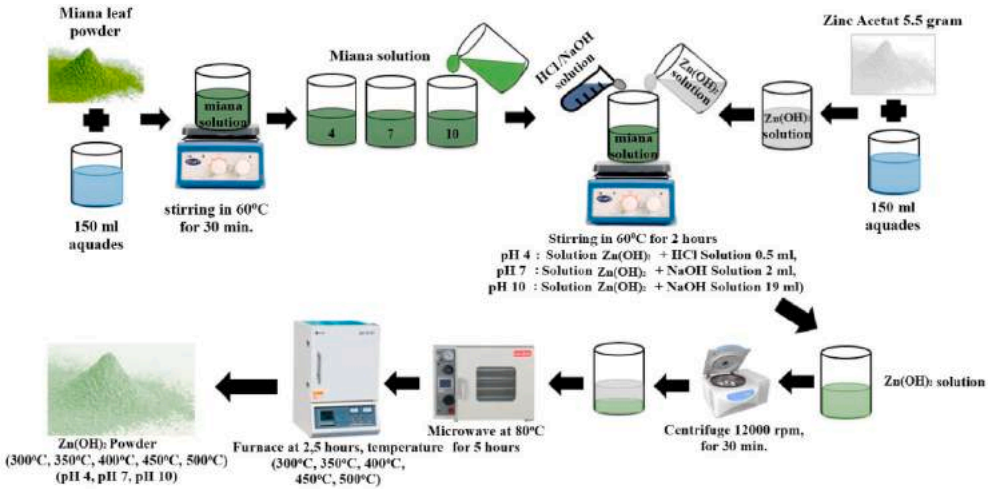

Fig. 1. Schematic diagram of green synthesis by using Miana (Coleus blumei Benth) leaf in production of Zn(OH)2 powder. (For interpretation of the references to color in this figure legend, the reader is referred to the Web version of this article.)

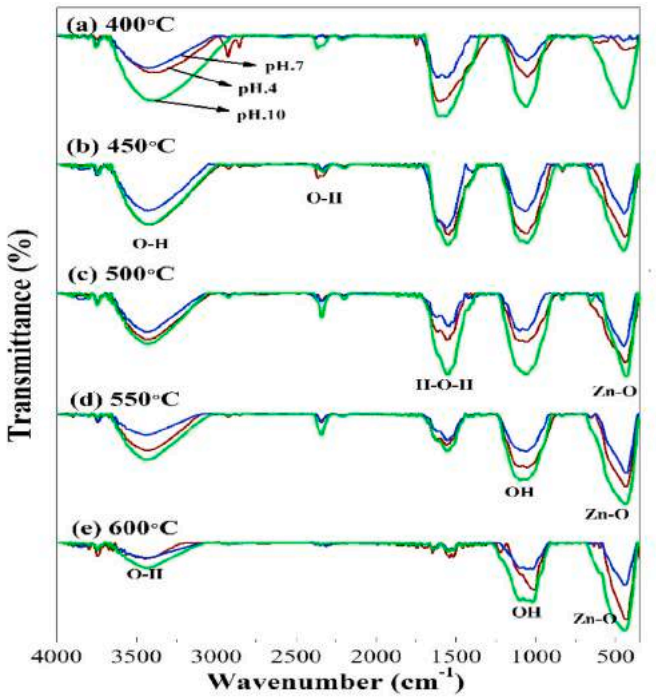

Fig. 2. FTIR Spectrum for various calcination temperature of Zn(OH)2 for pH 4, 7, and 10.

optical properties, dielectric function, and energy loss function of Zn (OH)2 nanocrystal from the quantitative analysis of Fourier transform infra-red (FTIR) spectroscopy spectra [32,33]. From the optical properties, the transverse optical (TO) and longitudinal optical (LO) phonon vibration mode can be determined. The KK dispersion relation was successfully used for analyzing the dielectric and optical properties of any kind of materials from the electron spectroscopy spectra as reported in Refs. [34–39]. By the quantitative analysis of the X-ray Diffraction (XRD) spectroscopy spectra, the structural properties determined and the ultra-violet visible (Uv–Vis) spectroscopy is used for determining the bandgap and the degradation performance. The effect of temperature and pH on the degradation performance was investigated and reported in detail.

2. Experimental

2.1. Material

Zinc Acetate dihydrate Zn(CH3COO)2 2H2O) (Merck), Sodium Hydroxide (NaOH) (Merck), Hydrogen Chloride (HCl) (Merck) and aquades pro analysis 99.99%.

2.2. Synthesis method

The Coleus blumei Benth (Miana) leaf was clean by using distilled water for removing dust and dirt and then dries it at room temperature for 5 days. The dry Coleus blumei Benth leaf was cutting for removing the stalks, blended to form the powder, and filtered 3 times for homogenous particle size. The powder was kept in the sample holder for further analysis.

The Coleus blumei Benth (Miana) leaf powder was mixing with distilled water and stirring for 30 min in 60 °C to form Miana solution then pour in three beakers for preparing three kinds of pH (4, 7, 10). Zinc solution was provided by mixing the zinc acetate with distilled water. Miana solution was stirred for 2 h and drops wise the zinc solution and NaOH or HCl solution until reached pH 4, 7, 10 which was labeled solution as Zn(OH)2 solution for pH 4, pH 7, and pH 10, respectively. The Zn(OH)2 solution was centrifuged at 12,000 rpm for 30 min. After centrifuge, the sediment was put into a cup and dried in a microwave with a temperature of 80 °C for 5 h. After that, the powder divided by 5 groups are 400 °C (group 1), 450 °C (group 2), 500 °C (group 3), 550 °C (group 4), and 600 °C (group 5) for calcination during 2.5 h to form Zn (OH)2 powder. For more detail of the synthesis method of Zn(OH)2 in this study are presented in Fig. 1.

2.3. Material characterization

Structural properties of Zn(OH)2 powder determined from the quantitative analysis of the X-ray diffraction (XRD) spectroscopy spectra (Shimadzu 7000) with CuKα radiation ($\lambda = 1{,}5405$ Å) in the range $15° \leq 2\theta \leq 80°$, operation at 30 kV and 10 mA. Fourier transform infrared (FTIR) spectroscopy was carried out on an IRPrestige-21 FTIR spectrometer (Shimadzu Corp.) equipped with a bright ceramic light source, a KBr beamsplitter, and a deuterated triglycine sulfate doped with L-alanine (DLATGS) detector. The FTIR spectra is used to study the functional group present in the crystalline structure, as well as the optical, dielectric, and energy loss function determined by applying KK relation. The Ultraviolet–visible (UV–Vis) absorption spectra for

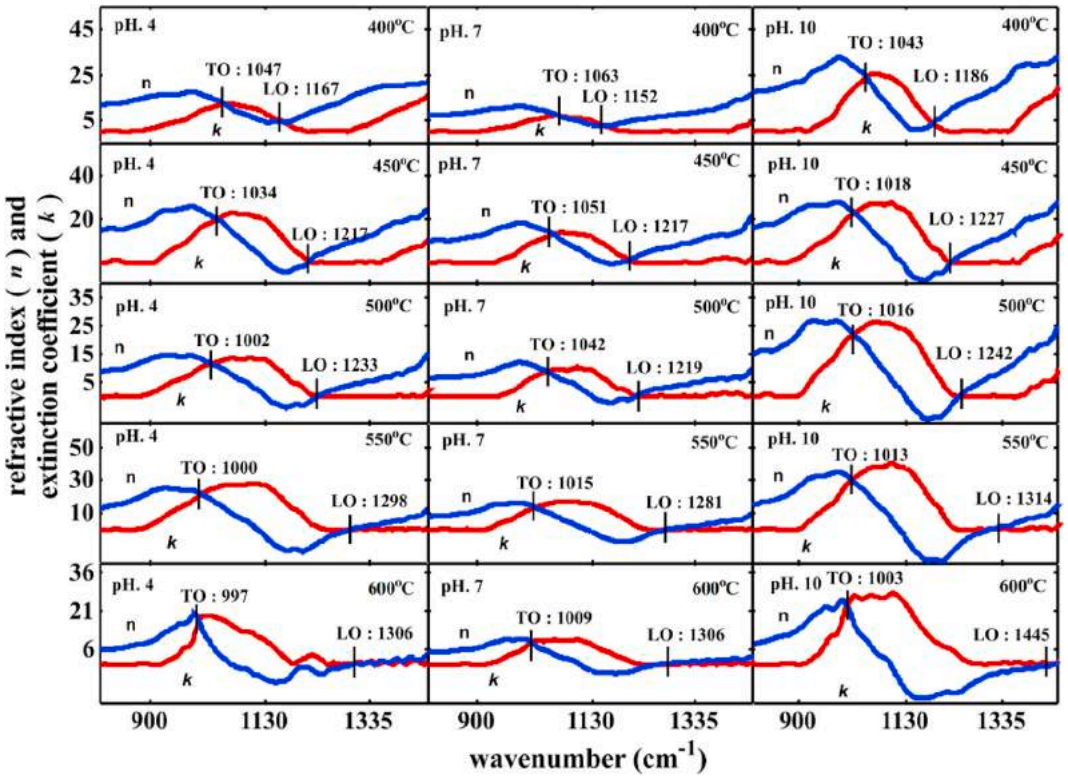

Fig. 3. The refractive index n and extinction coefficient k of Zn(OH)2 nanocrystal for various calcination temperature and pH, derived from the quantitative analysis of FTIR spectra (Fig. 2).

determining the absorption ability were recorded using a Shimadzu UV–Vis Spectrophotometer UV-1800.

2.4. Photocatalytic mechanism

We have used methylene blue as a model of contaminants in self-assembled equipment with halogen lamps (300 W, OSRAM 645, Germany) as a source of radiation for determining the photocatalytic activity of Zn(OH)2 as a function of pH and the calcination temperature. About 0.06 g of the Zn(OH)2 powder was suspended with 50 ml of methylene blue in a beaker. The suspension solution was applied in irradiation and then measured the absorption spectra for every 30 min by using a UV–Vis spectrometer. The degradation ability in the photocatalyst process by methylene blue as a model test of contaminant was determined by the equation as follows:

$$D(\%) = \frac{C_0 - C_t}{C_0} x100\% \quad (1)$$

Where $D(\%)$ is the percentage of degradation, C_0 is the initial absorbance, and C_t is the absorbance at the time t.

3. Results and discussion

FTIR spectra for Zn(OH)2 as a function of calcination temperature are shown in Fig. 2. The stretching vibration of *O*–H at the frequency 3417-3510 cm-1 due to the hydroxyl group. The intensity of these peaks was decreased with increasing the calcination temperature as we expected due to the evaporation effect. The effect of pH can be seen in the absorption spectra, the highest intensity for pH is 10 and the lowest is for pH 7, for pH 4 is in the middle probably due to the effect of vibrational at the surface state associated with O or H bonding formation movement parallel to the surface as reported in Refs. [40–42]. The absorption peak at 1560 cm-1 and in between 875 cm and 1 to 1015 cm-1 correspond to the H–*O*–H band bending and OH bond twisting, respectively. As can be seen clearly in Fig. 2 (b) the effect of temperature to the intensity of the H–*O*–H band is decrease with increasing the calcination temperature as we expected. At high temperature, the effect of the breaking covalent bond is dominant and the atoms going out from the materials which are reducing the intensity of some functional group [43,44]. The absorption peaks at 424-574 cm-1 are associated with the stretching of Zn–O which was increase with increasing the calcination temperature which is similar with the wavelength in between 875 cm and 1 to 1015 cm-1 for OH twisting indicated the Zn(OH)2 successfully synthesis and resulting strong bonding formation. That's mean that, the electronic structures at the surface state was modified [4,45–47]. The intensity of the functional group shows the highest for pH 10 may due to the ZnO cluster formation is highest (confirm later by the highest bandgap) [48,49]. pH 4 shows the intensity is in the middle between pH 10 and pH 7 probably due to the aggregation of AC play in decreasing surface roughness consequently increase hydrophobicity [48,49]. pH 7 is the lowest intensity probably due to the AC is in good order and bonding with Zn(OH)2 for some cluster but other cluster aggregation of AC still high consequently more decreasing surface roughness [48,49].

The optical properties (refractive index (n) and extinction coefficient (k)), dielectric function, and the energy loss function are usually used from quantitative analysis of electron spectroscopy spectra [34–36,38,50–53] and infra-red spectroscopy [32,33,54,55] by using KK relation. In this study, for these purposes, we used FTIR spectra by converted from the transmittance (T (ω)) to absorbance (A (ω)) to reflectance (R (ω)) as follows [32,33,50,54]:

$$A(\omega) = 2 - \log[T(\omega)\%] \quad (2)$$

$$R(\omega) = 100 - [T(\omega) + A(w)] \quad (3)$$

The reflectance (R (ω)) is used as an input parameter for determining the optical properties in the form of refractive index n(ω) and extinction coefficient k(ω) [32,33,50,54]:

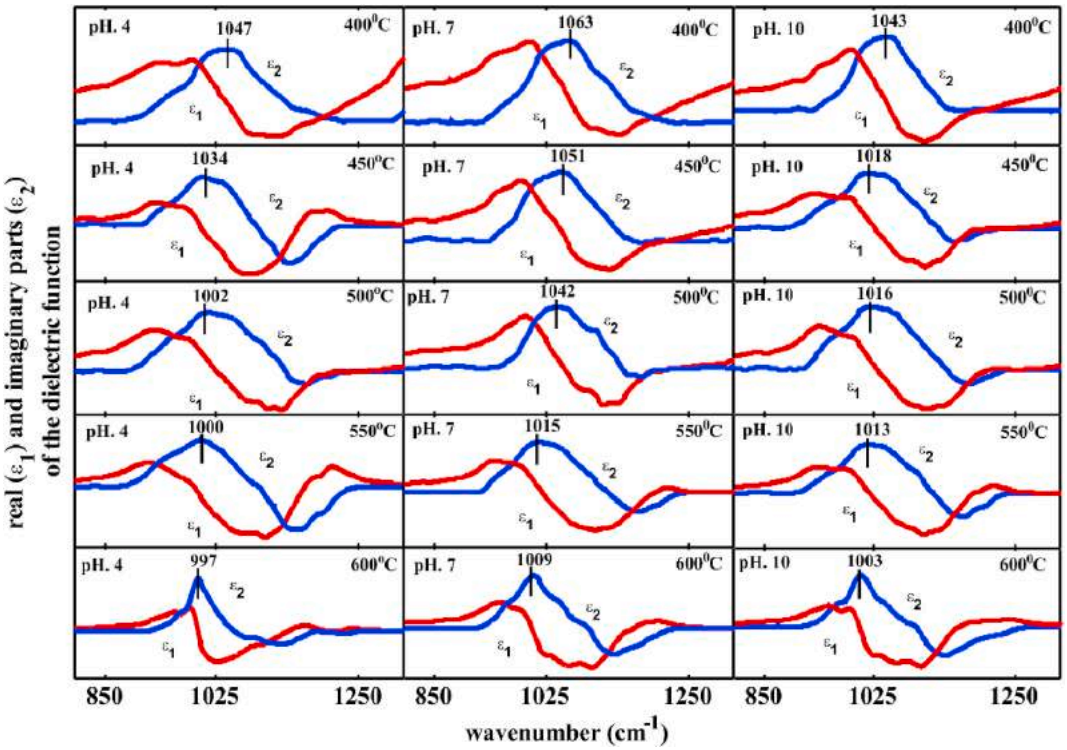

Fig. 4. The real part $\varepsilon 1$ and imaginary part $\varepsilon 2$ of dielectric function of Zn(OH)2 nanocrystal for various calcination temperature and pH.

Table 1
Longitudinal optical phonon mode (LO) and transverse optical phonon mode (LO) determined from Fig. 3, the main peak of real part ($\varepsilon 1$) and imaginary part ($\varepsilon 2$) of the dielectric function determined from Fig. 4 of Zn(OH)2, and the main peak of energy loss function (Im (-1/ε)) in this study.

pH	Temperature	TO	LO	ΔLO-TO	ε1	ε2	Im (−1/ε)
	0C	cm-1	cm-1	cm-1	cm-1	cm-1	cm-1
	400	1047	1167	120	987	1047	1167
	450	1034	1217	183	927	1034	1217
4	500	1002	1233	231	925	1002	1233
	550	1000	1298	298	908	1000	1298
	600	997	1309	312	979	997	1309
	400	1063	1152	89	1001	1063	1152
	450	1051	1206	155	987	1051	1206
7	500	1042	1219	177	985	1042	1219
	550	1015	1281	266	937	1015	1281
	600	1009	1309	300	949	1009	1309
	400	1043	1186	143	986	1043	1186
	450	1018	1227	209	935	1018	1227
10	500	1016	1242	226	931	1016	1242
	550	1013	1314	301	926	1013	1314
	600	1003	1445	442	950	1003	1445

$$n(\omega) = \frac{1 - R(\omega)}{1 + R(\omega) - 2\sqrt{R(\omega)}cos\phi(\omega)} \tag{4}$$

$$k(\omega) = \frac{2\sqrt{R(\omega)}sin\phi(\omega)}{1 + R(\omega) - 2\sqrt{R(\omega)}cos\phi(\omega)} \tag{5}$$

where ϕ(ω) is the phase change from the incident photon during travel inside the materials to the reflected photon in the processes of FTIR spectroscopy as follows:

$$\phi(\omega) = \frac{-\omega}{\pi}\int_0^{\infty} \frac{lnR(\omega') - lnR(\omega)}{\omega'^2 - \omega^2} d\omega' \tag{6}$$

By applying K–K relation the ϕ(ω) is the phase change become [32,33]:

$$\phi(\omega_j) = \frac{4\omega_j}{\pi}.\Delta\omega.\sum_i \frac{\ln\left(\sqrt{R(\omega)}\right)}{\omega_i^2 - \omega_j^2} \tag{7}$$

where $\Delta\omega = \omega_{i+1} - \omega_i$, j is a series of wavenumber, if j is an odd number so then i parts is 2,4,6,8, …,j-1,j+1 and while wavenumber j is an even, i parts is 1,3,5,7, …,j-1,j+1, …

Fig. 3 shows the n and k as a function of wavenumber for different pH from the left to the right 4, 7, and 10, and the calcination temperature from the first rows from 400 °C increase to the last rows for 600 °C. The intersection point at lower wavenumber indicated by TO is a transverse optical phonon mode and at higher wavenumber positions indicated by LO is longitudinal optical phonon mode [56]. The TO and LO of the Zn (OH)2 in these studies are presented in Table 1. From Fig. 3 and Table 1 shows clearly the effect of temperature to the optical phonon vibration for every pH (4, 7, and 10) the TO decreases and LO increases with increasing calcination temperature from 400 °C to 600 °C. For ex. pH 4 the TO and LO at 400 °C are 1047 cm-1 and 1167 cm-1, respectively and decrease to 997 cm-1 for TO and increase to 1309 cm-1 for LO at 600 °C may due to the lattice match to form a new phase of Zn(OH)2 structure increase in the Zn(OH)2 nanocrystal [57–59]. At low temperature for pH 4 and 7 the distance (Δ) between two optical phonon vibration mode Δ (LO-TO) is lower compared with the pH 10 probably due to the phase of Zn(OH)2 formation still incomplete in the lattice as the effect of OH vibrations consistent with the XRD spectra as can be seen clearly in Fig. 7.

Table 1 shows the distance (Δ) between two optical phonon vibration mode Δ (LO-TO) for various pH and calcination temperature. The highest value for pH 10 may due to the highest optical bandgap and some of the H2O loses in the lattice [48,49], the value decrease for pH 4 due to the OH atoms is not sitting properly in the lattice, and followed by pH 7 due to the cluster aggregation of AC is high consequently more defect in the lattice structure [48,49].

As can be seen in Fig. 3 and Table 1 the Δ (LO-TO) increased with increasing the calcination temperature for all pH indicated that the

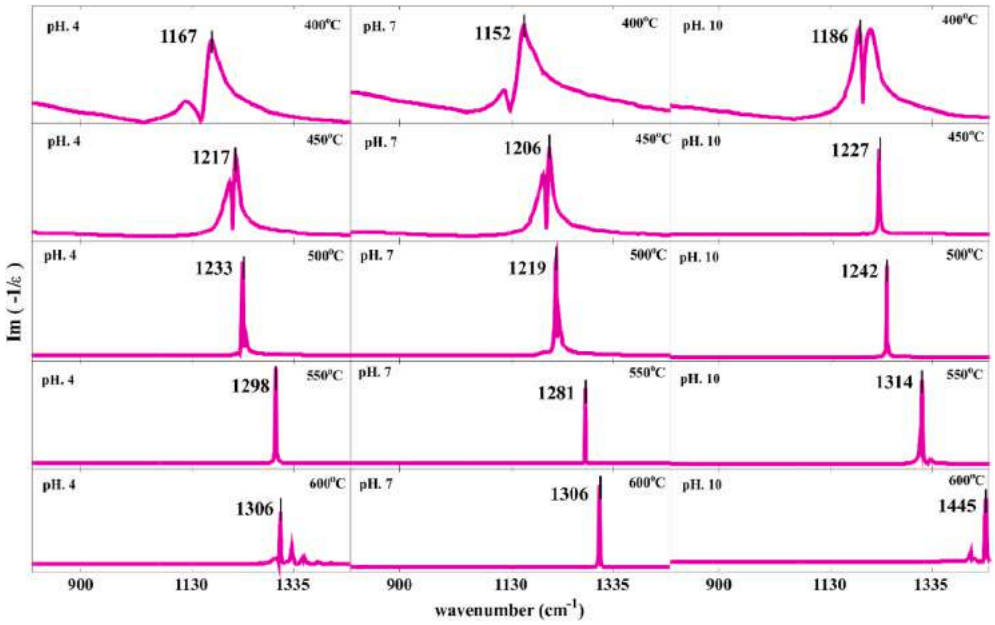

Fig. 5. The energy loss function Im $(-1/\varepsilon_1(\omega))$ derived from the dielectric function in Fig. 4 of Zn(OH)2 nanocrystal for various calcination temperature and pH.

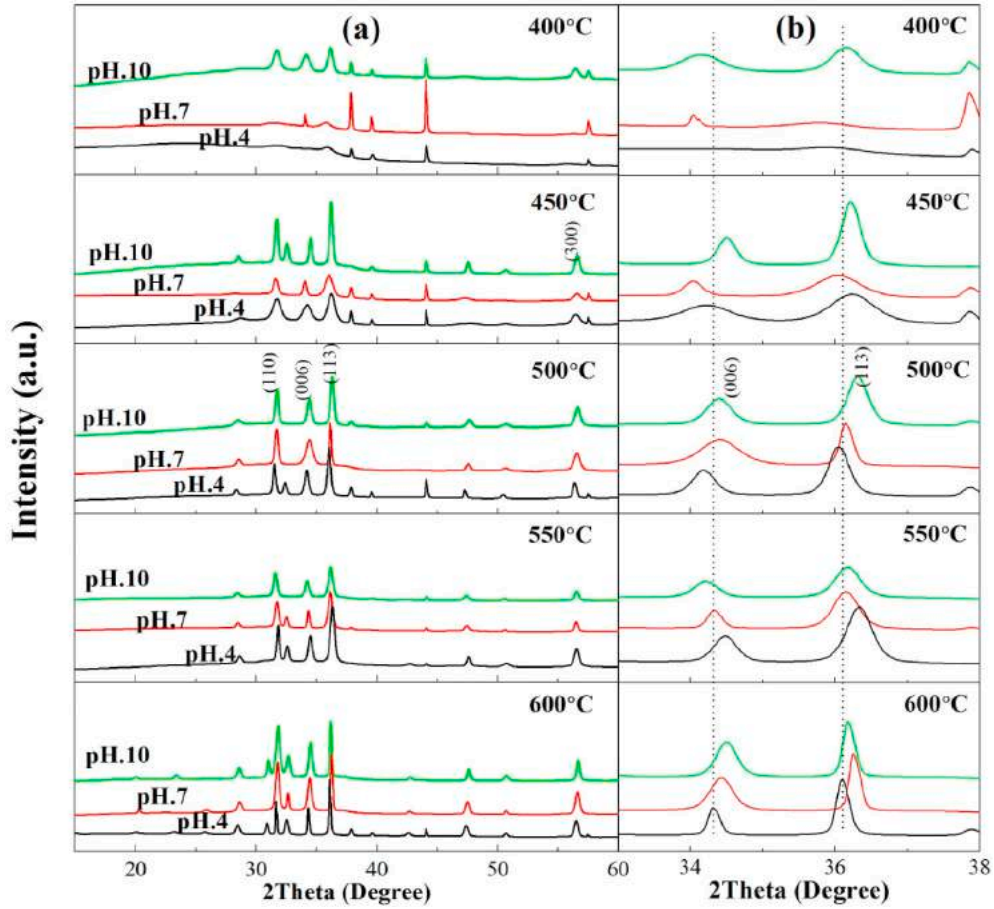

Fig. 6. The XRD full spectra for various calcination temperature of Zn(OH)2 for pH 4, 7, and 10 (a) and zoom of the diffraction peaks (006) and (113) (b).

strong and stable bonding connection by the covalent bond increase in the Zn(OH)2 nanocrystal [59–61]. The higher Δ (LO-TO) for pH 4 is 312 cm-1, for pH 7 is 300 cm-1, and for pH 10 is 442 cm-1 at calcination temperature 600 °C.

For the next analysis is use the n and k as the input parameter in determining the real part ($\varepsilon 1$) and imaginary part ($\varepsilon 2$) of the dielectric function as follows:

$$\varepsilon_1(\omega) = n^2(\omega) - k^2(\omega) \tag{8}$$

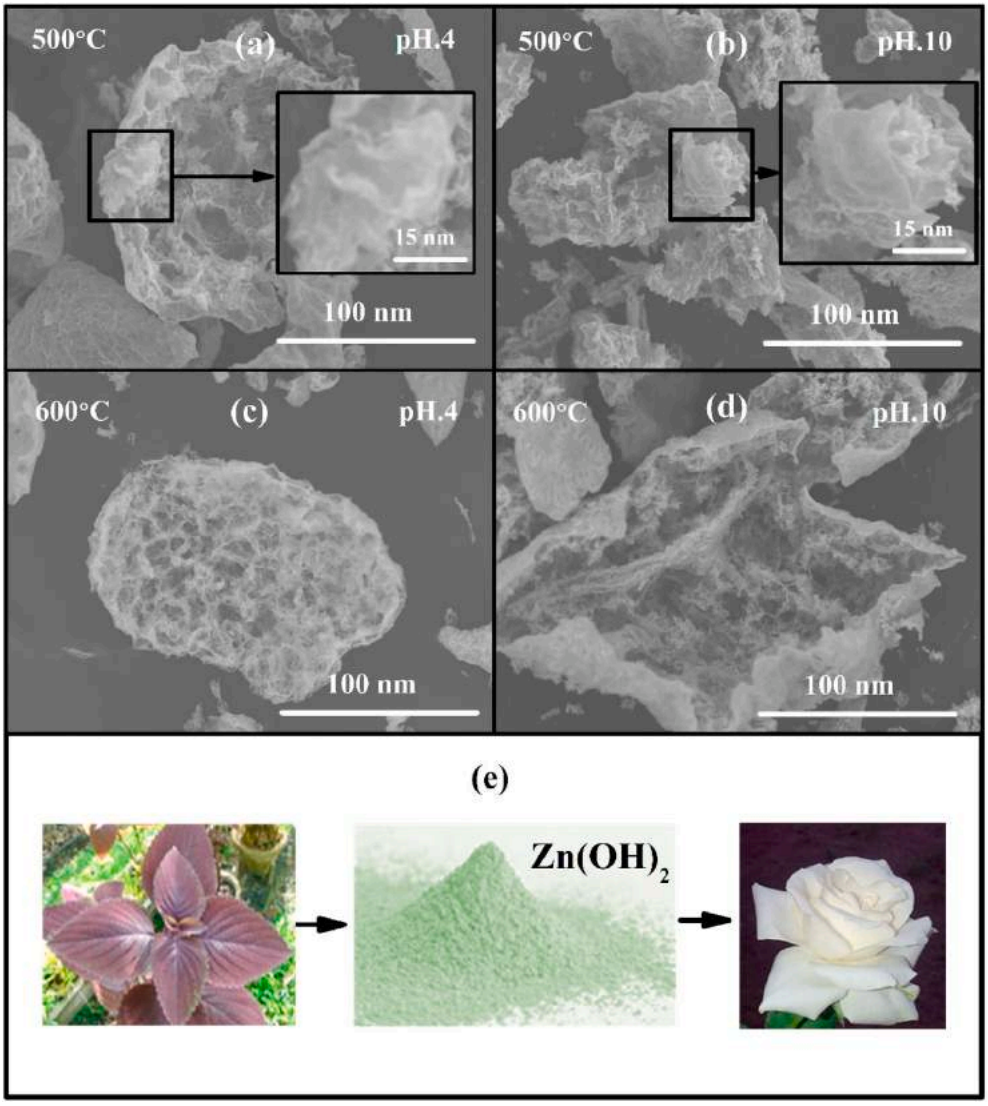

Fig. 7. SEM image from the flower-like structure of Zn(OH)2 for calcination temperature 500 °C (a, b) and 600 °C (c, d) for (pH 4 and 10), and (e) for illustration process from the leaf to the flower-like structure.

Table 2
Crystallite size, Lattice parameter (a and c), porosity, bond length, and dislocation density (1/D2) determined from the quantitative analysis of XRD spectra (Fig. 6) of Zn(OH)2 in this work.

Sample ID (Tempera ture-pH)	Crystallite Size (nm) (D)	Lattice Parameter (Å)				Volume (VCal)	Ratio (c/a)	Porosity (%)	Bond length (Å)	(1/D2) (nm-2)
		A	error	c	error					
400–4	28.73	3.45723	0.01506	5.53833	0.0295700	57.32800	1.60195	91.17	2.103961	0.0012
400–7	20.11	3.26238	0.00222	5.31213	0.0083244	48.96314	1.62830	91.41	1.995884	0.0025
400–10	13.94	3.48368	0.03044	5.33243	0.0928568	56.04453	1.53069	80.89	2.091739	0.0051
450–4	17.03	3.25032	0.00134	5.31476	0.0054682	48.62574	1.63515	94.60	1.991283	0.0034
450–7	13.89	3.26870	0.00136	5.27285	0.0047754	48.78957	1.61313	93.09	1.993649	0.0052
450–10	11.89	3.25728	0.00153	5.25650	0.0061686	48.29905	1.61377	92.08	1.986936	0.0071
500–4	15.43	3.26693	0.00125	5.26693	0.0049280	48.68196	1.61220	94.95	1.992195	0.0042
500–7	12.41	3.25620	0.00089	5.24836	0.0031590	48.19221	1.61181	94.84	1.985497	0.0065
500–10	10.89	3.25335	0.00103	5.24555	0.0041148	48.08206	1.61235	93.86	1.983976	0.0156
550–4	12.63	3.25180	0.00091	5.22222	0.0032700	47.82263	1.60595	95.76	1.980504	0.0063
550–7	11.01	3.26124	0.00077	5.23300	0.0021557	48.19988	1.60461	95.48	1.985724	0.0082
550–10	10.67	3.25237	0.00112	5.21285	0.0042123	47.75356	1.60279	95.21	1.979612	0.0161
600–4	18.72	3.26250	0.00124	5.23510	0.0045810	48.25659	1.60463	96.26	1.986502	0.0028
600–7	13.29	3.25224	0.00095	5.21684	0.0035928	47.78627	1.60408	96.05	1.980038	0.0057
600–10	11.69	3.25197	0.00126	5.20720	0.0050725	47.69015	1.60124	95.93	1.978768	0.0073

Table 3
Crystallite size, Bandgap, and rate constant (k) were determined by Eqs. (2), (7) and (8), respectively, for Zn (OH)2 in this work. Correlation coefficient determined from Fig. 11 (lower rows).

Sample ID	Crystallite Size (nm) (D)	Bandgap (eV)	Rate constant k min-1	Correlation coefficient values (R2)
Zn(OH)2 (pH.4)				
400	28,73	2.57	0.01033	0.93563
450	17,03	2.53	0.00984	0.99002
500	15,43	2.38	0.0116	0.94728
550	12,63	2.67	0.01025	0.99867
600	18,72	2.93	0.02372	0.99135
Zn(OH)2 (pH.7)				
400	20,11	2.93	0.01221	0.95923
450	13,89	2.54	0.00934	0.99545
500	12,41	2.57	0.01299	0.99256
550	11,01	2.73	0.01106	0.99963
600	13,29	2.95	0.02522	0.96373
Zn(OH)2 (pH.10)				
400	13,94	2.94	0.00793	0.98485
450	11,89	2.79	0.00532	0.96801
500	10.89	2.76	0.00563	0.99776
550	10.67	2.86	0.00638	0.99343
600	11,69	2.97	0.01499	0.98826

$$\varepsilon_2(\omega) = 2n(\omega)k(\omega) \tag{9}$$

For the real ($\varepsilon 1$) and imaginary ($\varepsilon 2$) part of the dielectric function are shown in Fig. 4 and the corresponding main peak positions are presented in Table 1.

The main peak position of $\varepsilon 2$ (ω) is used for confirmation of the TO phonon vibration modes as determined from the intersection point between n and k as shown in Fig. 3. The TO which was determined from Fig. 4 consistent with the main peak position of $\varepsilon 2$ (ω) indicated the effectiveness of experimental FTIR spectra in determining the optical and dielectric properties of the Zn(OH)2 nanocrystal. There are many studies also reported, the effectiveness of the quantitative analysis of electron spectroscopy spectra [34,36] in determining the optical and dielectric properties by using the KK dispersion relation.

The energy loss function Im $(-1/\varepsilon_1(\omega))=(\varepsilon_1(\omega))/((\varepsilon_1^2(\omega)+\varepsilon_2^2(\omega))$ determined from the dielectric function as an input parameter as shown in Fig. 5. The Im $(-1/\varepsilon_1(\omega))$ is usually described as the plasma frequency as reported in Refs. [34–36,46,51–53,56]. The Im $(-1/\varepsilon_1(\omega))$ is used for confirmation of the LO phonon vibration modes as determined from the intersection point between n and k as shown in Fig. 3. The plasma frequency for every pH is increased with increasing the calcination temperature as can be seen in Fig. 5 and Table 1, for ex. pH 4 at 400 °C is 1167 increase to 1309 cm-1 at 600 °C indicated that the lattice match and the covalent bond with strong and stable bonding formation increase in the Zn(OH)2 nanocrystal [57,59,61].

Fig. 6 shows the XRD spectrum of Zn(OH)2 synthesis by various

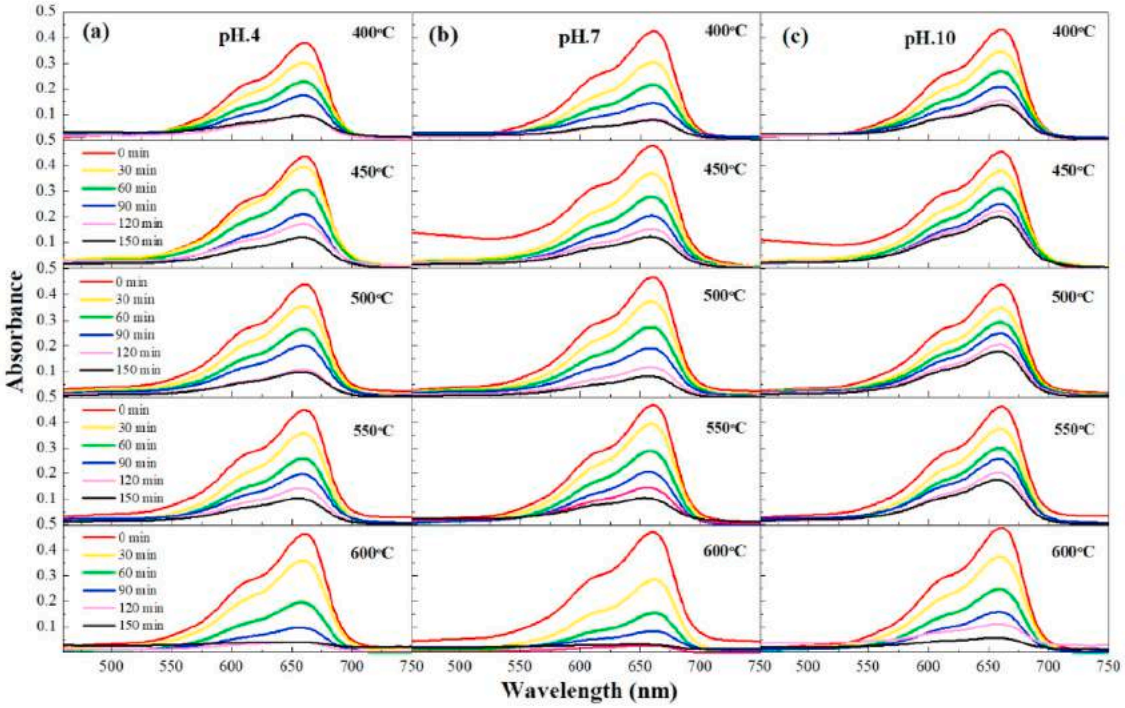

Fig. 8. The absorbance intensity of the main peak from Uv–Vis spectra as a function of irradiation time for various pH and calcination temperature of Zn(OH)2 nanocrystal.

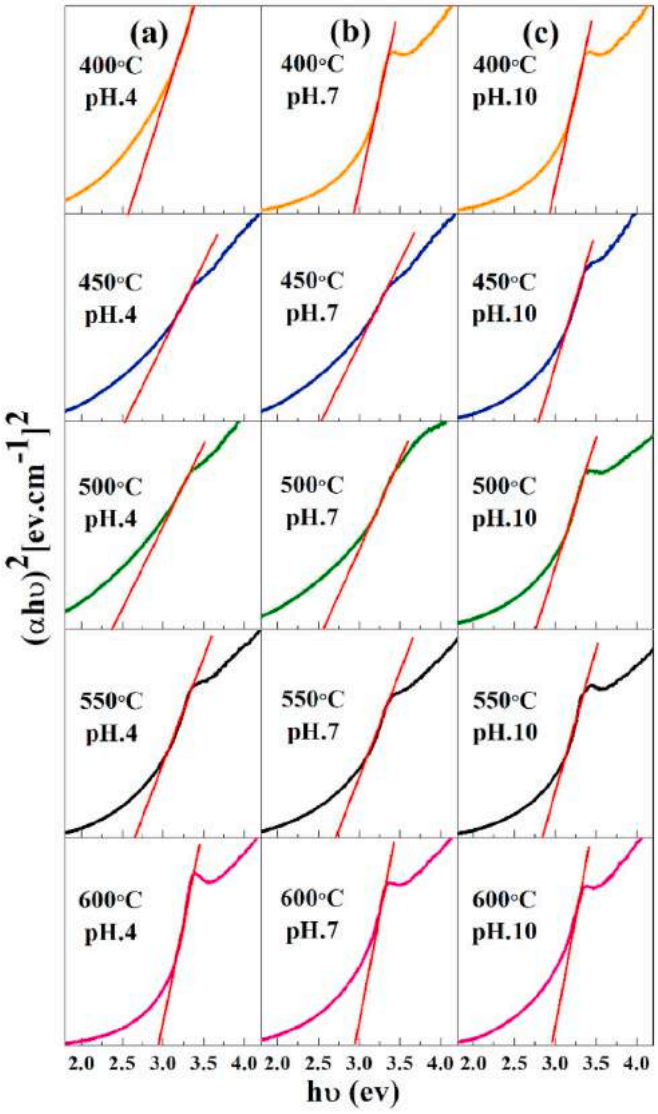

Fig. 9. Band gap of Zn(OH)2 for various pH (4, 7, 10) determined from Uv–Vis spectroscopy by using Equation (14) (band gap value of all sample in this study can be seen in Table 3).

calcination temperatures and pH. For low-temperature 400 °C shows diffraction peaks are depending on the pH, for pH 4 and 7 shows broad diffraction peaks (113) while for pH 10 clearly shows three main diffraction peaks of Zn(OH)2 are (110), (006), and (113) but for the temperature >400 °C, the diffraction peaks plane sharper are (110), (006), and (113) for all pH. As reported in Ref. [44], the main diffraction peaks for Zn(OH)2 nanoparticle is (110) and (113). The shifted of the all peak for different pH at the same temperature clearly seen in Fig. 6 (b), probably correspond to the different structural properties or due to the Zn atom successfully bonding with OH forming Zn(OH)2 nanocrystal which were consistent with FTIR spectra in Fig. 2. The OH bonding with Zn can be identified by the presence of the peaks at lower and higher 2θ positions than that of (110) crystal plane. These peaks probably indicated the hydroxyl group (OH) attached on the surface of ZnO in the form of Zn(OH)2 which comes from the extract leave as reported in Refs. [62,63]. These peaks were affected to the surface structure at the high temperature indicated by changes in the shape and the intensity as reported in Ref. [22]. For the calcination temperature increase up to 600 °C, the transformation phase occurred due to the H2O loses increase from the Zn(OH)2 which indicated that, the cluster of ZnO nanocrystal is dominant. The OH bonding with Zn in the form of Zn(OH)2 still exists were indicated by the small peaks close to (110) crystal plane.

The full width at half maximum (FWHM) of the diffraction peak for material in this study in nanometer size was decreased with increasing the calcination temperature. The structural properties; lattice parameter, volume, porosity, bond length, and dislocation density as a result of quantitative analysis of XRD spectra are shown in Table 2. Some of the peaks were shift as the effect of pH and the annealing temperature probably due to the migration of atoms to find a stable position [64,65]. The shifts and the intensity of XRD change as the effect of pH and calcination temperature may due to the phase Zn(OH)2 formation in lattice structure is still incomplete [66,67]. The lattice parameter and the bond length for calcination temperature >400 °C is similar although for the different pH. For 400 °C, the lattice parameter and the bond length are high for pH 4 and pH 10 indicated that, the leaf extract, NaOH, and HCl successfully modified the surface state of ZnO nanocrystal to become Zn(OH)2 as can be seen clearly in the XRD spectra and FTIR spectra.

The Debye-Scherrer formula was used for calculation of the average crystallite size D by using the following the equation [68]:

$$D = \frac{k\lambda}{B\cos\theta} \tag{10}$$

where k is a constant (0.9), λ is an X-ray wavelength (0.154 nm), B is the full width at half the maximum (FWHM), and θ is the diffraction angle. The results of the calculation of D as a function of calcination temperature and pH can be seen in Tables 2 and 3. The crystallite size of nanoparticle was decreased with increasing the calcination temperature from 400 °C to 600 °C. For the temperature <600 °C the bonding between Zn with H2O still dominating which may protect solidification between the crystal, consequently decrease the crystallite size. For 600 °C, the H2O loses from Zn(OH)2 increase sharply resulting the ZnO cluster formation is dominant [69].

The defect presents in the crystal structure identified from the dislocation density which were determined from the crystallite size D and the corresponding result presented in Table 2. The dislocation density is lower for pH 4 and increases with increasing the pH to 10, for the effect of temperature also clearly shows an increase with increasing the calcination temperature for the same pH. The higher calcination temperature and high pH may facilitate the reorientations of the crystal growth were influenced to increasing the amount of the covalent bond connection in the crystal structure. The crystallite size, lattice parameter, volume, porosity, bond length, and dislocation density are shown in Table 2.

$$V = \frac{\sqrt{3}}{2}a^2c \tag{11}$$

$$u = \frac{a^2}{3c^2} + 0.25 \tag{12}$$

$$L = \sqrt{0.3a^2 + \left(\frac{1}{2} - u\right)^2 c^2} \tag{13}$$

Lattice volume (V), internal parameter (u), and bond length (L) were determined based on the quantitative analysis of XRD spectra. The porosity of the Zn(OH)2 in this study shows >80% which was calculated based on equations (4)–(6) in Ref. [45], indicated that the pore is high potential to be used as a trap of the charged particle. Table 2 shows the c/a value for Zn(OH)2 is 1.633 shows the best agreement for c/a in Ref. [70] and also for lattice volume shows in the range of 47.18 Å to 49.34 Å indicated that, the Zn(OH)2 in this study was grown properly. The bond length for Zn(OH)2 in this study in the range of 1.97 Å up to 2.10 Å is quite similar reported in Ref. [71].

Morphological analysis of Zn(OH)2 synthesis from Coleus blumei Bent is shown in Fig. 7. The nano flower-like structure for temperature 500 °C come from ZnO for each temperature and pH. The OH probably

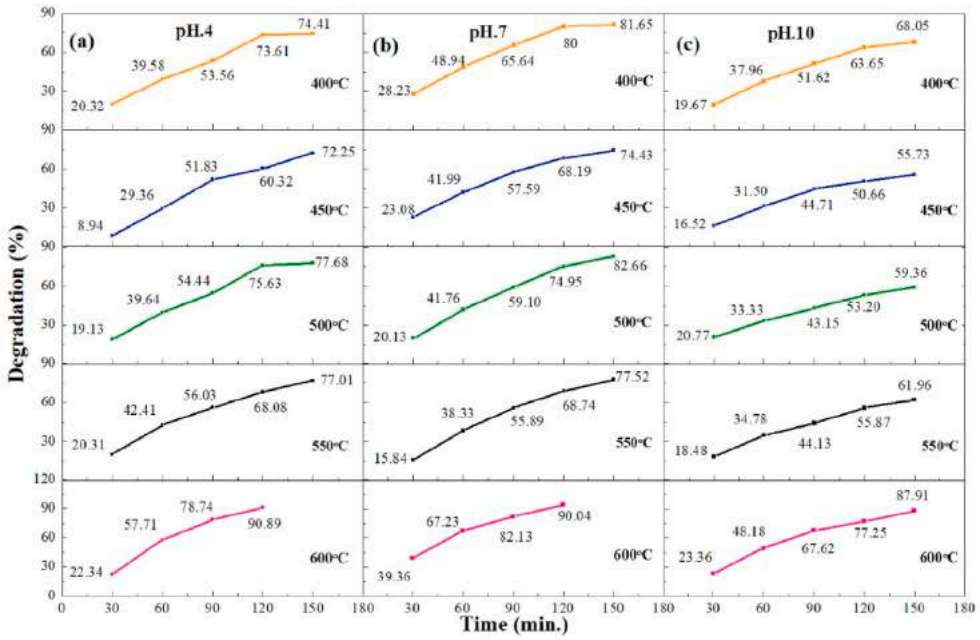

Fig. 10. Degradation performance (%) of Zn(OH)2 nanocrystal as a function of irradiation time for various calcination temperature (a) pH 4 (b) pH 7 (c) pH 10 determined by using equation (1).

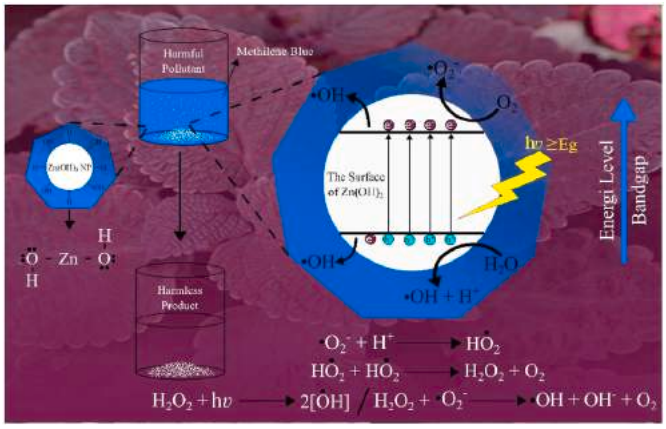

Fig. 11. Schematic illustration of the impurity on the surface of the Zn(OH)2 nanocrystal (left side) and photo-catalytic activity by the charge carrier (e− and h+) in producing harmless product (right side).

attached in the surface of flower petal by white color to form Zn(OH)2 structure which was consistent with the crystal structure from the XRD spectra in Fig. 6. The SEM surface image for the same magnification 100 nm shows for the 600 °C (pH 4), the morphological small flower-like structure formed is clearer (Fig. 7 (a and b)), the bonding is better, and the surface structure which is supported by the lack of defects. The effect of temperature at 600 °C shows significant reduce the size of the flower (Fig. 7 (c)) but for pH 10 at 600 °C shows destroy the petal flower-like structure as can be seen clearly in Fig. 7 (d).

There are two ways for determining the bandgap with high accuracy, first, by quantitative analysis of reflection electron energy loss spectroscopy (REELS) spectra from the low loss region [38,72] and the second, by using quantitative analysis absorption spectra from the Uv–Vis spectroscopy [73,74]. In this study, we have applied the Tauc-plot relation by quantitative analysis from the absorption spectrum (Fig. 8) and the corresponding bandgap values are shown in Table 3. The Tauc-plot plot relation was presented in the form of absorption coefficient (α) as follows:

$$\alpha = \frac{A\left(h\nu - E_g\right)^{1/2}}{h\nu} \tag{14}$$

where A is the coefficient of proportionality, h is the Planck constant, v is the frequency of light and Eg is the bandgap. The bandgap was determined from the cross point in the x-axis [63] indicated by the red line in Fig. 9.

Fig. 9 and Table 3 shows the bandgap decrease for 400 °C–500 °C may due to the amount of oxygen present in Zn(OH)2 nanocrystal increases which can be attributed to the Moss-Burstein effect [75,76]. For the temperature at 500 °C probably all of the Zn, O, and H atoms are in the right position at the lattice structure. For the temperature >500 °C, some of the impurity from H2O goes out from the lattice and the remaining atoms re-arranged for new strong and stable bonding connections in the lattice structure that increases the bandgap [77]. The absorbance intensity as a function of irradiation time for various pH and calcination temperatures can be seen in Fig. 8 and the corresponding results of degradation performance are presenting in Fig. 10. For 600 °C shows the best temperature indicated by the degradation performance faster than other temperature for all pH.

The hydroxyl group (OH) attached at the surface of ZnO and become Zn(OH)2 but at the high temperature, the ZnO cluster is dominant which potential for keeping the bandgap in the visible region. The illustration of OH was attached at the surface of ZnO as shown in Fig. 11 (left side). The Zn(OH)2 lattice introduces a new covalent bond with oxygen and hydrogen which may strong and stable connection, lead to enhance electron-hole generation [78]. The electron at the valence band is gains the energy during the irradiation process as shown in Fig. 11 (right side). The strong and stable covalent bond in Zn(OH)2 can suppress the recombination of the carrier. The step process for the Zn(OH)2 nanocrystal to be used in the photo-catalysts are [79–81]:

1. Electron in the valence band (VB) gains the energy from the photo (irradiation) for excitation to the conduction band (CB) and remains a hole in the VB.
2. The electron in the CB will be adsorbed the oxygen atoms in the form of O2 and produce O2*- radicals.

Table 4
Comparison of the degradation performance (%) of the previously reported for materials: Bi12TiO20 [16], ZrO2 doped Eu [20], ZnO doped Eu and Mg [22], CdTe/TiO2 [21] based photo-catalysts with Zn(OH)2 in this work.

Sample ID	Concentration	Catalyst dosage	Source	Time (min.)	Degradation (%)	Organic dye	Lamp Power (Watt)	Reference
Bi12TiO20	15 mg/L	15 mg	Sunlight	120	98	Methyl Orange	300	W. GuO et al., 2014 [16]
CdTe/TiO2	10 mg/L	10 mg	UV light	120	55	*p*-Nitrophenol	300	Hui Feng et al., 2013 [21]
ZnO (PNP)	20 mg/L	20 mg	Sunlight	60	48	*p*-Nitrophenol	–	P. K. Labhane et al., 2018 [22]
Mg/ZnO (PNP)	20 mg/L	20 mg	Sunlight	60	70.52	*p*-Nitrophenol	–	
ZnO (IC)	20 mg/L	20 mg	Sunlight	60	60	Indigo Carmine	–	
Mg/ZnO (IC)	20 mg/L	20 mg	Sunlight	60	62.32	Indigo Carmine	–	
ZrO2 (1.0% Eu)	20 mg/L	100 mg	Sunlight	150	64.5	Indigo Carmine	150	E. S. Agorku et al., 2015 [20]
Zn(OH)2 (pH.4)								
400	35 mg/L	35 mg	Sunlight	150	74.41	Methyl blue	300	Present
450	35 mg/L	35 mg	Sunlight	150	72.25	Methyl blue	300	Present
500	35 mg/L	35 mg	Sunlight	150	77.68	Methyl blue	300	Present
550	35 mg/L	35 mg	Sunlight	150	77.01	Methyl blue	300	Present
600	35 mg/L	35 mg	Sunlight	120	90.89	Methyl blue	300	Present
Zn(OH)2 (pH.7)								
400	35 mg/L	35 mg	Sunlight	150	81.65	Methyl blue	300	Present
450	35 mg/L	35 mg	Sunlight	150	74.43	Methyl blue	300	Present
500	35 mg/L	35 mg	Sunlight	150	82.66	Methyl blue	300	Present
550	35 mg/L	35 mg	Sunlight	150	77.52	Methyl blue	300	Present
600	35 mg/L	35 mg	Sunlight	120	90.04	Methyl blue	300	Present
Zn(OH)2 (pH.10)								
400	35 mg/L	35 mg	Sunlight	150	68.05	Methyl blue	300	Present
450	35 mg/L	35 mg	Sunlight	150	55.73	Methyl blue	300	Present
500	35 mg/L	35 mg	Sunlight	150	59.36	Methyl blue	300	Present
550	35 mg/L	35 mg	Sunlight	150	61.96	Methyl blue	300	Present
600	35 mg/L	35 mg	Sunlight	150	87.91	Methyl blue	300	Present

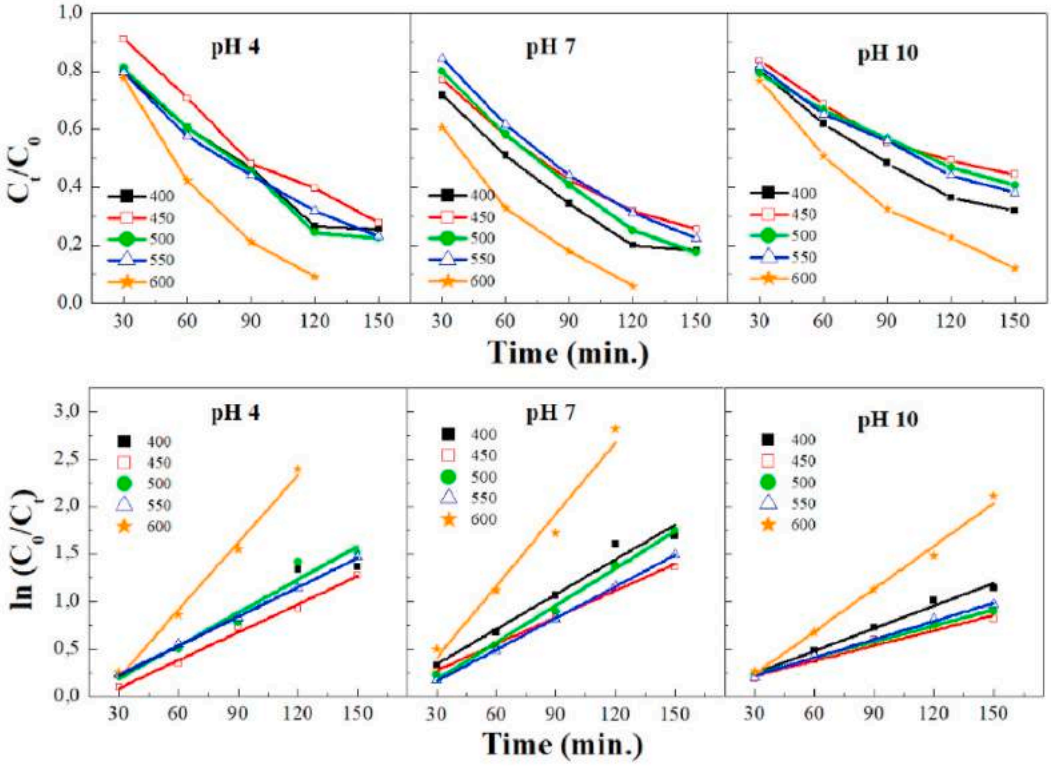

Fig. 12. Photocatalytic activity (Ct/C0) first row and ln (C0/Ct) of Zn(OH)2 nanocrystal as a function of irradiation time for various calcination temperature (a) pH 4 (b) pH 7 (c) pH 10 determined by using equation (15).

3. The hole at the VB moves to the surface and disturbs the H2O molecule to produce H+ and OH × radicals.
4. The O2*- as a result of the electron in CB bonding with H+ as a result of hole in the VB produced HO2*. If there are two of the HO2* combine together resulting H2O2 and O2.
5. There are two ways for H2O2 to participate in the photocatalytic activity; by gaining the energy from the irradiation to form 2OH × and by bonding with O2*- resulting OH*, OH- and O2.
6. These OH × radicals as an oxidizing agent for participating in photocatalytic activity by attacking the molecule from the pollutant

absorbed on the surface of Zn(OH)2 producing intermediates composite and converted to CO2 and H2O.

The degradation rate constant (k) in the photocatalytic reaction was calculated by the following equation:

$$\ln\left(\frac{C_0}{C_t}\right) = kt \quad (15)$$

Where C0 is the initial concentration and Ct is the concentration at the time t, and k is the first-order rate constant. The rate constants k values were measured from the slope of the equation. As can be seen clearly in Table 4, the novelty and photo-degradation efficiency in this study compared with other references [16,20–22]. For the effect of pH shows the highest efficiency is for pH 7 and the lowest is for pH 10 may due to the defect from the interstitial of atoms or the anionic from methylene blue attracted to the positive charge at the surface of Zn(OH)2 [67,82]. The best calcination temperature is 600 °C as can be seen clearly in Fig. 12 indicated by the rate of the degradation performance is faster than the other temperature. This is due to the strong and stable covalent bond that make during irradiation is easily generated the carrier (electron and hole) and also suppress the recombination of the carrier which is consistent with the analysis optical and dielectric properties from the FTIR spectra. The charge (electron and hole) as the result of the process of excitation after gains the energy during the irradiation process is responsible for accelerating the photocatalytic performance [83]. Enhancing the charge separation under influence of the irradiation, the lattice match and stable bonding connection are needed [79,80] which was consistent with the Δ (LO-TO) and plasma frequency from the quantitative analysis of FTIR spectra. For high calcination temperature, the photocatalyst process is higher probably due to the presence of the electron scavenger which can diffuse from the surface of Zn(OH)2 nanocrystal [82,84]. We have compared our results for showing the novelty in this study with Ref. [16] for Methyl orange [21,22], for *p*-Nitrophenol [19], for Indigo Carmine as can be seen in Table 4.

It can be concluded that, at high-temperature calcination for pH neutral (7), the formation of the lattice match and stable bonding connection are important. These formations are effective parameters for separation of the charge consequently the photocatalytic performance is enhanced. Lattice match, strong, and the stable bonding connection indicated by: the higher distance between two optical phonon vibration, the higher wavenumber of the plasma frequency, and the lower main peak of the dielectric function, and higher bandgap energy. For higher calcination temperature and high pH were facilitated the reorientation of the crystal growth that influenced to increasing amount of the covalent bond in the crystal structure, consequently increase the photocatalytic performance.

4. Conclusion

Quantitative analysis of the optical, electronic, and structural properties of Zn(OH)2 nanocrystal for photocatalytic applications were successfully carried out from the spectra of FTIR, Uv–Vis, and XRD, respectively. From the analysis of FTIR spectra shows the presence of bonding OH, H–*O*–H, *O*–H, and Zn–O indicated Zn(OH)2 nanocrystal was formed. The distance between two optical phonon vibration modes Δ (LO-TO) and the plasma frequency increases with increasing the calcination temperature for all pH indicated that the lattice match, strong and stable bonding connection by the covalent bond increases in the Zn(OH)2 nanocrystal. The dislocation density is lower for pH is 4 and increase with increasing the pH to 10, for the effect of temperature was increase with increasing the calcination temperature for the same pH which facilitate the reorientation of the crystal growth influenced to the increasing the amount of the stable bonding connection in the crystal structure. The bandgap increases with increasing the calcination temperature, for >500 °C and some of the impurity from H2O goes out from the lattice forming ZnO, and the remaining atoms re-arranged for new strong, and stable bonding connection in the lattice structure. The best calcination temperature is 600 °C and pH 7 due to the rate of the degradation performance is faster than the other temperature and pH. The distance between two kinds of phonon vibration, plasma frequency, dielectric function, and the bandgap strongly influences the lattice match and stable bonding connection, consequently enhanced the photocatalytic performance. FTIR spectra show effective ways for determining the optical, dielectric properties, and energy loss function of Zn(OH)2 as a function of pH and calcination temperature which is fundamental properties for the photocatalytic activity. For high-temperature calcination and higher pH shows the formation of a lattice match, strong and stable bonding connection is an important and effective parameter for separation and suppress recombination of the charge for the acceleration of the photocatalytic performance.

CRediT authorship contribution statement

Nurlaela Rauf: Writing - original draft. **Sultan Ilyas:** Writing - original draft. **Heryanto Heryanto:** Writing - original draft, Software, Validation. **Roni Rahmat:** Writing - original draft. **Ahmad Nurul Fahri:** Writing - original draft. **Mufti Hatur Rahmi:** Writing - review & editing, Writing, reviewing, and correction of the original draft, Writing - original draft. **Dahlang Tahir:** Software, Validation, Writing, reviewing, Writing - review & editing, and correction of the original draft, Writing - original draft.

Declaration of competing interest

The authors declare that they have no known competing financial interests or personal relationships that could have appeared to influence the work reported in this paper.

Acknowledgment

This work was supported by the PD (Penelitian Dasar) and PT (Penelitian Terapan) funded by the Indonesia Government (Kemenristek/BRIN) grants: 1516/UN4.22/PT.March 01, 2020.

References

[1] G. Nam, J.Y. Leem, Fast-response photoconductive ultraviolet light detectors fabricated using high-quality ZnO films obtained by plasma-assisted molecular beam epitaxy, Ceram. Int. 43 (15) (2017) 11981–11985.
[2] K.H. Park, G.D. Han, B.J. Kim, E.H. Kang, J.S. Park, J.H. Shim, H.D. Park, Effects of atomic layer deposition conditions on the formation of thin ZnO films and their photocatalytic characteristics, Ceram. Int. 45 (15) (2019) 18823–18830.
[3] B.C. Lin, C.S. Ku, H.Y. Lee, A.T. Wu, Epitaxial growth of ZnO nanorod arrays via a self-assembled microspheres lithography, Appl. Surf. Sci. 414 (2017) 212–217.
[4] R. Anugrahwidya, N. Yudasari, D. Tahir, Optical and structural investigation of synthesis ZnO/Ag Nanoparticles prepared by laser ablation in liquid, Mater. Sci. Semicond. Process. 105 (2020) 104712.
[5] X. Li, Z. Hu, J. Liu, D. Li, X. Zhang, J. Chen, J. Fang, Ga doped ZnO photonic crystals with enhanced photocatalytic activity and its reaction mechanism, Appl. Catal. B Environ. 195 (2016) 29–38.
[6] H. Mandal, S. Shyamal, P. Hajra, B. Samanta, P. Fageria, S. Pande, C. Bhattacharya, Improved photoelectrochemical water oxidation using wurtzite ZnO semiconductors synthesized through simple chemical bath reaction, Electrochim. Acta 141 (2014) 294–301.
[7] M.R.A. Cruz, O.C. Sanchez, E.L. Hipólito, L.M.T. Martínez, ZnO thin films deposited by RF magnetron sputtering: effects of the annealing and atmosphere conditions on the photocatalytic hydrogen production, Int. J. Hydrogen Energy 43 (22) (2018) 10301–10310.
[8] H. Agarwal, S.V. Kumar, S. Rajeshkumar, A review on green of zinc oxide nanoparticles-An eco-friendly approach, Resource-Efficient Technologies 3 (2017) 406–413.
[9] H. Mirzaei, M. Darroudi, Zinc oxide nanoparticles: biological synthesis and biomedical application, Ceram. Int. 43 (2016) 907–914.
[10] S. Ahmed, S. Annu, A. Chaudhry, S. Ikram, A review on biogenic synthesis of ZnO nanoparticles using plant extracts and microbes: a prospect towards green chemistry, J. Photochem. Photobiol. B Biol. 166 (2016) 272–284.

[11] P. Jamdagni, P. Khatri, J.S. Rana, Green synthesis of zinc oxide nanoparticles using flower extract of Nyctanthes arbor-tristis and their antifungal activity, J. King Saud Univ. Sci. 30 (2) (2016) 168–175.

[12] S. Yedurkar, C. Maurya, P. Mahanwar, Biosynthesis of Zinc Oxide nanoparticles using Ixora Coccinea leaf extract-A green approach, Open J. Synth. Theor. Appl. 5 (2016) 1–14.

[13] P. Singh, Y.J. Kim, D. Zhang, D.C. Yang, Biological synthesis of nanoparticles from plants and microorganism, Trends Biotechnol. 34 (7) (2016) 588–599.

[14] T.V. Surendra, S.M. Roopan, N.A. Al-Dhabi, M.V. Arasu, G. Sarkar, K. Suthindhiran, Vegetable peel waste for the production of ZnO nanoparticles and its toxicological efficiency, antifungal, hemolytic, and antibacterial activities, Nanoscale Research Letters 11 (2016) 546.

[15] S.T. Fardood, A. Ramazani, S. Moradi, P.A. Asiabi, Green synthesis of zinc oxide nanoparticles using Arabic gum and photocatalytic degradation of direct blue 129 dye under visible light, J. Mater. Sci. Mater. Electron. 28 (18) (2017) 13596–13601.

[16] W. Guo, Y. Yang, Y. Guo, Y. Jia, H. Liu, Y. Guo, Self assembled hierarchical Bi12TiO20–graphene nanoarchitectures with excellent simulated sunlight photocatalytic activity, Phys. Chem. Chem. Phys. 16 (6) (2013) 2705–2714.

[17] M.N. Subramaniam, P.S. Goh, N. Abdullah, W.J. Lau, B.C. Ng, A.F. Ismail, Adsorption and photocatalytic degradation of methylene blue using high surface area titanate nanotubes (TNT) synthesized via hydrothermal method, J. Nanoparticle Res. 19 (2017) 220.

[18] S. Minallah, E. Pervaiz, M.U. Yousaf, M.B.K. Niazi, L. Honghong, M. Yang, Ternary adsorbent photocatalyst hybrid (APH) nanomaterials for improved abstraction of tetracycline from water, Separ. Sci. Technol. 55 (15) (2019) 2623–2641, https://doi.org/10.1080/01496395.2019.1640742.

[19] M. Rani, U. Shanker, Degradation of traditional and new emerging pesticides in water by nanomaterials: recent trends and future recommendation, International Journal of Enviromental Science and Technology 15 (6) (2017) 1347–1380.

[20] E.S. Agorku, A.T. Kuvarega, B.B. Mamba, A.C. Pandey, A.K. Mishra, Enhanced visible-light photocatalytic activity of multi-elements-doped ZrO2 for degradation of indigo carmine, J. Rare Earths 33 (5) (2015) 498–506.

[21] H. Feng, Tran T. ThanhThuy, L. Chen, L. Yuan, Q. Cai, Visible light-induced efficiently oxidative decomposition of p-Nitrophenol by CdTe/TiO2 nanotube arrays, Chem. Eng. J. 215–216 (2013) 591–599.

[22] P.K. Labhane, S.H. Sonawane, G.H. Sonawane, S.P. Patil, V.R. Huse, Influence of Mg doping on ZnO nanoparticles decorated on graphene oxide (GO) crumpled paper like sheet and its high photo catalytic performance under sunlight, J. Phys. Chem. Solid. 114 (2017) 71–82.

[23] H.S. Choo, S.M. Lam, J.C. Sin, A.R. Mohamed, An efficient Ag2SO4-deposites ZnO in photocatalytic removal of indigo carmine and phenol under outdoor light irradiation, Desalination and Water Treatment 57 (30) (2015) 14227–14240.

[24] X. Liu, L. Zhao, H. Lai, X. Zhang, Z. Yi, Highly effective degradation of p-Nitrophenol over MoS2 under visible light illumination, Catal. Lett. 147 (8) (2017) 2153–2159.

[25] J.Z. Marinho, L.F. de Paula, E. Longo, A.O.T. Patrocinio, R.C. Lima, Effect of Gd3+ doping on structural and photocatalytic properties of ZnO obtained by facile microwave-hydrotermal method, SN Applied Sciences 1 (4) (2019) 359.

[26] Md A.I. Molla, M. Furukawa, I. Tateishi, H. Katsumata, S. Kaneco, Fabrication of Ag-doped ZnO by mechanochemical combustion method and their application into photocatalytic famotidine degradation, Journal of Environmental Science and Health, Part A 54 (9) (2019) 914–923.

[27] M. Roosta, M. Ghaedi, R. Sahraei, M.K. Purkait, Ultrasonic assisted removal of sunset yellow from aqueous solution by zinc hydroxide nanoparticle loaded activated carbon: optimized experimental design, Mater. Sci. Eng. C 52 (2015) 82–89.

[28] R. Kamaraj, A. Pandiarajan, S. Vasudevan, S. Vasudevan, Facile one-pot electrosynthesis of zinc hydroxide for the adsorption of hazardous 2-(2-methyl-4-chlorophenoxy) propionic acid (MCPP) from water and its modelling studies, Journal of Environmental Chemical Engineering 6 (2018) 2017–2026.

[29] R. Kamaraj, A. Pandiarajan, S. Jayakiruba, Mu Naushad, S. Vasudevan, Kinetics, thermodynamics and isotherm modeling for removal of nitrate from liquids by facile one-pot electrosynthesized nano zinc hydroxide, J. Mol. Liq. 215 (2016) 204–211.

[30] M. Karakawa, T. Sugahara, Y. Hirose, K. Suganuma, Y. Aso, Thin film of amorphous zinc hydroxide semiconductor for optical devices with an energy-efficient beneficial coating by metal organic decomposition process, Sci. Rep. 8 (2018) 10839, https://doi.org/10.1038/s41598-018-27953-6.

[31] O. Altuntasoglu, Y. Matsuda, S. Ida, Y. Matsumoto, Syntheses of zinc oxide and zinc hydroxide single nanosheets, Chem. Mater. 22 (2010) 3158–3164.

[32] Gh H. Khorrami, A.K. Zak, A. Kompany, R. Yousefi, Optical and structural properties of X-doped (X=Mn, Mg, and Zn) PZT nanoparticle by Kramers-Kronig and size strain plot methods, Ceram. Int. 38 (2002) 5683–5690.

[33] M. Ghasemifard, S.M. Hosseini, Gh H. Khorrami, Synthesis and structure of PMN-PT ceramic nanopowder free from pyrochlore phase, Ceram. Int. 35 (2009) 2899–2905.

[34] D. Tahir, J. Kraaer, S. Tougaard, Electronic and optical properties of Fe, Pd, and Ti studied by reflection electron energy loss spectroscopy, J. Appl. Phys. 115 (2014) 243508.

[35] D. Tahir, S.K. Oh, H.J. Kang, S. Tougaard, Composition dependence of dielectric and optical properties of Hf-Zr-silicate thin films grown on Si (100) by atomic layer deposition, Thin Solid Films 116 (2016) 425–430.

[36] D. Tahir, S.K. Oh, H.J. Kang, S. Tougaard, Quantitative analysis of reflection electron energy loss spectra to determine electronic and optical properties of Fe-Ni alloy thin films, J. Electron. Spectrosc. Relat. Phenom. 206 (2016) 6–11.

[37] D. Tahir, E.K. Lee, H.L. Kwon, S.K. Oh, H.J. Kang, S. Heo, E.H. Lee, J.G. Chung, J. C. Lee, S. Tougaard, Electronic and optical properties of GIZO thin film grown on SiO2/Si substrates, Surf. Interface Anal. 42 (2010) 906–910.

[38] D. Tahir, E.H. Choi, Y.J. Cho, S.K. Oh, H.J. Kang, H. Jin, S. Heo, J.G. Chung, J. C. Lee, S. Tougaard, Electronic and optical properties of La-aluminate dielectric thin films on Si (100), Surf. Interface Anal. 42 (2010) 1566–1569.

[39] S. Heo, D. Tahir, J.G. Chung, J.C. Lee, K. Kim, J. Lee, H. Lee, G.S. Park, S.K. Oh, H. J. Kang, P. Choi, B.D. Choi, Band alignment of atomic layer deposited (HfZrO4) 1-x (SiO2) x gate dielectrics on Si (100), Appl. Phys. Lett. 107 (2015) 182101.

[40] M. Isik, N.M. Gasanly, The defect state of Yb-doped ZnO nanoparticles using thermoluminescence study, Mater. Sci. Semicond. Process. 100 (2019) 29–34.

[41] D.A.G. Casamachin, J.R.D.L. Rosa, C.J.L. Ortiz, D.A.D. Rio, D.X.M. Vergas, G.A. F. Escamila, N.E.D. Guzman, V.M.O. Medina, E.M. Valazquez, Visible-light photocatalytic degradation of acid violet 7 dye in continuous annular reactor using ZnO/PPy photocatalyst: synthesis, characterization, mass transfer effect evaluation and kinetic analysis, Chem. Eng. J. 373 (2019) 325–337.

[42] L.V. Trandafilovic, D.J. Jovanovic, X. Zhang, S. Ptasinska, M.D. Dramicanin, Enhanced photocatalytic degradation of methylene blue and methylene orange by ZnO:Eu nanoparticles, Appl. Catal. B Environ. 203 (2016) 740–752.

[43] M. Nasirian, C.F.B. Lecompte, M. Mehrvar, Photocatalytic efficiency of Fe2O3/TiO2 for the degradation of typical dyes in textile industries: effects of calcination temperature and UV-assisted thermal synthesis, J. Environ. Manag. 196 (2017) 487–498.

[44] Z.N. Kayani, F. Saleemi, I. Batool, Effect of calcination temperature on the properties of ZnO nanoparticles, Appl. Phys. A 119 (2) (2015) 713–720.

[45] D. Tahir, S. Ilyas, B. Abdullah, B. Armynah, K. Kim, H.J. Kang, Modification in electronic, structural, and magnetic properties based on composition of composites Copper (II) Oxide (CuO) and carbonaceous material, Mater. Res. Express 6 (2018), 035705.

[46] D. Tahir, S. Ilyas, B. Abdullah, B. Armynah, H.J. Kang, Electronic properties of composite iron (II, III) oxide (Fe3O4) carbonaceous absorber materials by electron spectroscopy, J. Electron. Spectrosc. Relat. Phenom. 229 (2018) 47–51.

[47] S. Fatimah, S.M. Bilqis, Isnaeni, D. Tahir, Luminescence properties of carbon dots synthesis from sugar for enhancing glows in paints, Mater. Res. Express 6 (2019), 095006.

[48] A. Kamgar, S. Hassanajili, Super-hydrophobic Fe3O4@SiO2@MPS nanoparticles for oil remediation: the influence of pH and concentration on clustering phenomenon and oil sorption, J. Mol. Liq. 315 (2020) 113709.

[49] Y. Yang, S. He, Y. Ye, X. Cao, H. Liu, Z. Wu, J. Yue, H. Sun, Enhanced hydrophobicity of soybean protein isolate by low-pH shifting treatment for the sub-micron gel particles preparation, Ind. Crop. Prod. 151 (2020) 112475.

[50] M.J. Iqbal, N. Yaqub, B. Sepiol, B. Ismail, A study of the influence of crystallite size on the electrical and magnetic properties of CuFe2O4, Mater. Res. Bull. 46 (2011) 1837–1842.

[51] D. Tahir, H.L. Kwon, H.C. Shin, S.K. Oh, H.J. Kang, S. Heo, J.G. Chung, J.C. Lee, S. Tougaard, Electronic and optical properties of Al2O3/SiO2 thin films grown on Si substrate, J. Phys. Appl. Phys. 43 (2010) 255301.

[52] H.C. Shin, D. Tahir, S. Seo, Y. Rama, Denny, S.K. Oh, H.J. Kang, S. Heo, J.G. Chung, J.C. Lee, S. Tougaard, Reflection electron energy loss spectroscopy for ultrathin gate oxide materials, Surf. Interface Anal. 44 (6) (2012) 623–627.

[53] D. Tahir, S. Tougaard, Electronic and optical properties of selected polymers studied by reflection electron energy loss spectroscopy, J. Appl. Phys. 111 (2012), 054101.

[54] L. Legana, T. Leskovar, M. Cresnar, F. Cavalli, D. Innocenti, P. Ropret, Non-invasive reflection FTIR characterization of archaeological burnt bones: reference database and case studies, J. Cult. Herit. 41 (2019) 13–26.

[55] R. Zamiri, H.M. Chenari, H.F. Moafi, Mehdi Shabani, S.A. Salehizadeh, A. Rebelo, J. Suresh Kumar, M.P.F. Graça, M.J. Soares, J.M.F. Ferreira, Ba-doped ZnO nanostructure: X-ray line analysis and optical properties in visible and low frequency infrared, Ceram. Int. 42 (11) (2016) 12860–12867.

[56] S. Suryani, H. Heryanto, R. Rusdaeni, A.N. Fahri, D. Tahir, Quantitative analysis of diffraction and infra-red spectra of composite cement/BaSO4/Fe3O4 for determining correlation between attenuation coefficient, structural and optical properties, Ceram. Int. 46 (2020) 18601–18607.

[57] M. Ghasemifard, E. Fathi, M. Ghamari, The effect of Fe3+-doped on structure and optical properties of mesoporous Al2O3/SiO2 composite, Mater. Sci. Semicond. Process. 42 (2016) 349–353.

[58] S.A.M. Lima, F.A. Sigoli, M. Jafelicci, M.R. Davolos, Luminescent properties of lattice defect correlation in zinc oxide, Int. J. Inorg. Mater. 3 (2001) 749–754.

[59] M. Ghasemifard, S. Tohidi, R. Karimzadeh, Effects of Pb-doping on phase structural and optical properties of CdZnS nano-powders, J. Electron. Sci. Technol. 3 (2013) 16.

[60] V. Lucarini, J.J. Saarinen, K.E. Peiponen, E.M. Vartiainen, Kramers–Kronig Relations in Optical Materials Research, Springer, Berlin, Heidelberg, New York, 2004.

[61] R.G. Greenler, Reflection absorption infrared spectroscopy and the structure of molecular adsorbents on metal surfaces, J. Chem. Phys. 51 (2000) 381–403.

[62] J. Lv, M. Fang, K. Cheng, Z. Chai, Thermal evolution of impurities and hydroxyl groups in ZnO nanocrystals, J. Lumin. 209 (2019) 146–149.

[63] P. Madhusudan, Y. Wang, B.N. Chandrashekar, W. Wang, J. Wang, J. Miao, R. Shi, Y. Liang, G. Mi, C. Cheng, Nature inspired ZnO/ZnS nanobranch-like composites, decorated with Cu(OH)2 clusters for enhanced visible-light photocatalytic hydrogen evolution, Appl. Catal. B Environ. 253 (2019) 379–390.

[64] D. Tahir, H.L. Kwon, H.C. Shin, S.K. Oh, H.J. Kang, S. Heo, J.G. Chung, J.C. Lee, S. Tougaard, Electronic and optical properties of Al2O3/SiO2 thin films grown on Si substrate, J. Phys. Appl. Phys. 43 (2010) 255301.

[65] D. Tahir, N.S. Park, D.S. Yang, H.J. Kang, Electronic properties of Ga-In-Zn-O (GIZO) thin films: effect of post-annealing, J. Electron. Spectrosc. Relat. Phenom. 234 (2019) 1–4.
[66] C.A.J. Paez, J.A. Navio, M.C. Hidalgo, M. Macias, ZnO and Pt-ZnO photocatalyst: characterization and photocatalytic activity assessing by means of three substrates, Catal. Today 313 (2018) 12–19.
[67] J. Ungula, B.F. Dejene, H.C. Swart, Effect of pH on the structural, optical and morphological properties of Ga-doped ZnO nanoparticles by reflux precipitation method, Physica B 535 (2018) 251–257.
[68] S. Ilyas, Heryanto, B. Abdullah, D. Tahir, X-ray diffraction analysis of nanocomposite Fe3O4/activated carbon by Williamson-Hall and size-strain plot methods, Nano-Structures and Nano-Objects 20 (2019) 100396.
[69] R.P.P. Singh, I.S. Hudiara, S.B. Rana, Effect of calcination temperature on the structural, optical and magnetic properties of pure and Fe-doped ZnO nanoparticles, Materials Science-Poland 34 (2) (2016) 451–459.
[70] M. Goswami, N.C. Adhikary, S. Bhattacharjee, Effect of annealing temperatures on the structural and optical properties of zinc oxide nanoparticles prepared by chemical precipitation method, Optik 158 (2018) 1006–1015.
[71] J. Singh, S. Sharma, S. Soni, S. Sherma, R.C. Singh, Influence of different milling media on structural, morphological and optical properties of the ZnO nanoparticles synthesized by ball milling process, Mater. Sci. Semicond. Process. 98 (2019) 29–38.
[72] S. Heo, D. Tahir, J.G. Chung, J.C. Lee, K.H. Kim, J. Lee, H.L. Lee, G.S. Park, S.K. Oh, H.J. Kang, P. Choi, B.D. Choi, Band alignment of atomic layer deposited (HfZrO4) 1-x(SiO2)x gate dielectrics on Si (100), Appl. Phys. Lett. 107 (2015) 182101.
[73] H.C. Shin, D. Tahir, S. Seo, Y. Rama, Denny, S.K. Oh, H.J. Kang, S. Heo, J.G. Chung, J.C. Lee, S. Tougaard, Reflection electron energy loss spectroscopy for ultrathin gate oxide materials, Surf. Interface Anal. 44 (6) (2012) 623–627.
[74] K. Varunkumar, R. Hussain, G. Hegde, A.S. Ethiraj, Effect of calcination temperature on Cu doped NiO nanoparticles prepared via wet-chemical method: structural, optical and morphological studies, Mater. Sci. Semicond. Process. 66 (2017) 149–156.
[75] L. He, Z. Tong, Z. Wang, M. Chen, N. Huang, W. Zhang, Effects of calcination temperature and heating rate on the photocatalytic properties of ZnO prepared by pyrolysis, J. Colloid Interface Sci. 509 (2017) 448–456.
[76] S. Kumar, A.K. Ojha, Room temperature ferromagnetism in undoped and Mn doped t-ZrO2 nanostructures originated due to oxygen vacancy and effect of Mn doping on its optical properties, Mater. Chem. Phys. 169 (2016) 13–20.
[77] S. Klubnuan, S. Suwanboon, P. Amornpitoksuk, Effect of optical bandgap energy, band tail energy and particle shape on photocatalytic activities of different ZnO nanostructures prepared by a hydrothermal method, Opt. Mater. 53 (2016) 134–141.
[78] M. Samadi, M. Zirak, A. Naseri, E. Khorashadizade, A.Z. Moshfegh, Recent progress on doped ZnO nanostructures for visible-light photocatalysis, Thin Solid Films 605 (2016) 2–19.
[79] K.M. Lee, C.W. Lai, K.S. Ngai, J.C. Juan, Recent developments of zinc oxide based photocatalyst in water treatment technology: a review, Water Res. 88 (2015) 428–448.
[80] I. Kazeminezhad, A. Sadollahkhani, Influence of pH on the photocatalytic activity of ZnO nanoparticles, J. Mater. Sci. 27 (5) (2016) 4206–4215.
[81] A. Kajbafvala, H. Ghorbani, A. Paravar, J.P. Samberg, E. Kajbafvala, S. K. Sadrnezhaad, Effects of morphology on photocatalytic performance of zinc oxide nanostructures synthesis by rapid microwave irradiation method, Superlattice. Microst. 51 (2012) 512–522.
[82] C. Lai, M.M. Wang, G.M. Zeng, Y.G. Liu, D.L. Huang, C. Zhang, R.Z. Wang, P. Xu, M. Cheng, C. Huang, H.P. Wu, L. Qin, Synthesis of surface molecular imprinted TiO2/graphene photocatalyst and its highly efficient photocatalytic degradation of target pollutant under visible light irradiation, Appl. Surf. Sci. 390 (2016) 368–376.
[83] R.K. Sahu, K. Ganguly, T. Mishra, M. Mishra, R.S. Ningthoujam, S.K. Roy, L. C. Pathak, Stabilization of intrinsic defect at high temperatures in ZnO nanoparticles by Ag Modification, J. Colloid Interface Sci. 366 (2011) 8–15.
[84] B. Ulum, S. Ilyas, A.N. Fahri, I. Mutmainna, M.A. Anugrah, N. Yudasari, E. B. Demmalino, D. Tahir, Composite carbon-lignin/zinc oxide nanocrystalline ball-like hexagonal mediated from jatropha curcas L leaf as photocatalyst for industrial dye degradation, J. Inorg. Organomet. Polym. Mater. 30 (2020) 4905–4916.